



Article

<https://doi.org/10.1038/s41467-023-35916-3>

Exclusive detection of volatile aromatic hydrocarbons using bilayer oxide chemiresistors with catalytic overlayers

Received: 10 September 2022

Seong-Yong Jeong^{1,2,3}✉, Young Kook Moon^{1,3}, Joseph Wang² & Jong-Heun Lee^{1,4}

Accepted: 6 January 2023

Published online: 25 January 2023

Check for updates

The accurate detection and identification of volatile aromatic hydrocarbons, which are highly toxic pollutants, are essential for assessing indoor and outdoor air qualities and protecting humans from their sources. However, real-time and on-site monitoring of aromatic hydrocarbons has been limited by insufficient sensor selectivity. Addressing the issue, bilayer oxide chemiresistors are developed using Rh–SnO₂ gas-sensing films and catalytic CeO₂ overlayers for rapidly and cost-effectively detecting traces of aromatic hydrocarbons in a highly discriminative and quantitative manner, even in gas mixtures. The sensing mechanism underlying the exceptional performance of bilayer sensor is systematically elucidated in relation to oxidative filtering of interferants by the CeO₂ overlayer. Moreover, CeO₂-induced selective detection is validated using SnO₂, Pt–SnO₂, Au–SnO₂, In₂O₃, Rh–In₂O₃, Au–In₂O₃, WO₃, and ZnO sensors. Furthermore, sensor arrays are employed to enable pattern recognition capable of discriminating between aromatic gases and non-aromatic interferants and quantifying volatile aromatic hydrocarbon classifications.

With rapid societal and environmental changes, monitoring and managing new synthetic odors and various airborne chemicals have become increasingly important^{1–6}. Volatile aromatic hydrocarbons (VAHs) such as benzene (B), toluene (T), ethylbenzene (E), xylene (X), and styrene (S) are major hazardous indoor and outdoor air pollutants in the petroleum and chemical industries, vehicles, and urban and residential areas (Fig. 1a)^{7–10}. For instance, exposure to trace concentrations of benzene can cause leukemia, and methylbenzene (i.e., toluene and xylene), ethylbenzene, and styrene are representative health hazards that induce headaches, dizziness, nausea, and vomiting^{7,8,10–12}. Furthermore, such hazardous VAHs are generally found at low concentrations (i.e., several ppm) in both indoor and outdoor environments^{8,10,13}. Thus, the development of highly sensitive and selective techniques for detecting traces of VAHs must be developed for evaluating air quality in real-time and on-site.

Conventional VAH detection relies on bulky, expensive, complex, and time-consuming methods and instruments including gas chromatography–mass spectrometry (GC–MS)¹⁴, proton transfer reaction–mass spectrometry (PTR–MS)¹⁵, fluorescent probes¹⁶, and photoacoustic spectrometers¹⁷, which hamper instantaneous, portable, and cost-effective gas monitoring. In this regard, various chemiresistors including oxide semiconductors^{1,18–26}, carbon nanotubes (CNTs)²⁷, graphene-based materials (rGOs)²⁸, transition metal dichalcogenides (TMDs)²⁹, and transition metal carbides and nitrides (MXenes)³⁰ have attracted considerable attention as alternative platforms due to their high gas response, rapid response, simple structure, good stability, and easy miniaturization. Among them, oxide semiconductor chemiresistors with higher operation temperatures are advantageous for VAHs detection because sufficient thermal activation can facilitate a sensing reaction between target gas and surface

¹Department of Materials Science and Engineering, Korea University, Seoul 02841, Republic of Korea. ²Department of Nanoengineering, University of California, San Diego, La Jolla, CA 92093, USA. ³These authors contributed equally: Seong-Yong Jeong, Young Kook Moon. ⁴Deceased: Jong-Heun Lee. ✉e-mail: jeong7460@korea.ac.kr

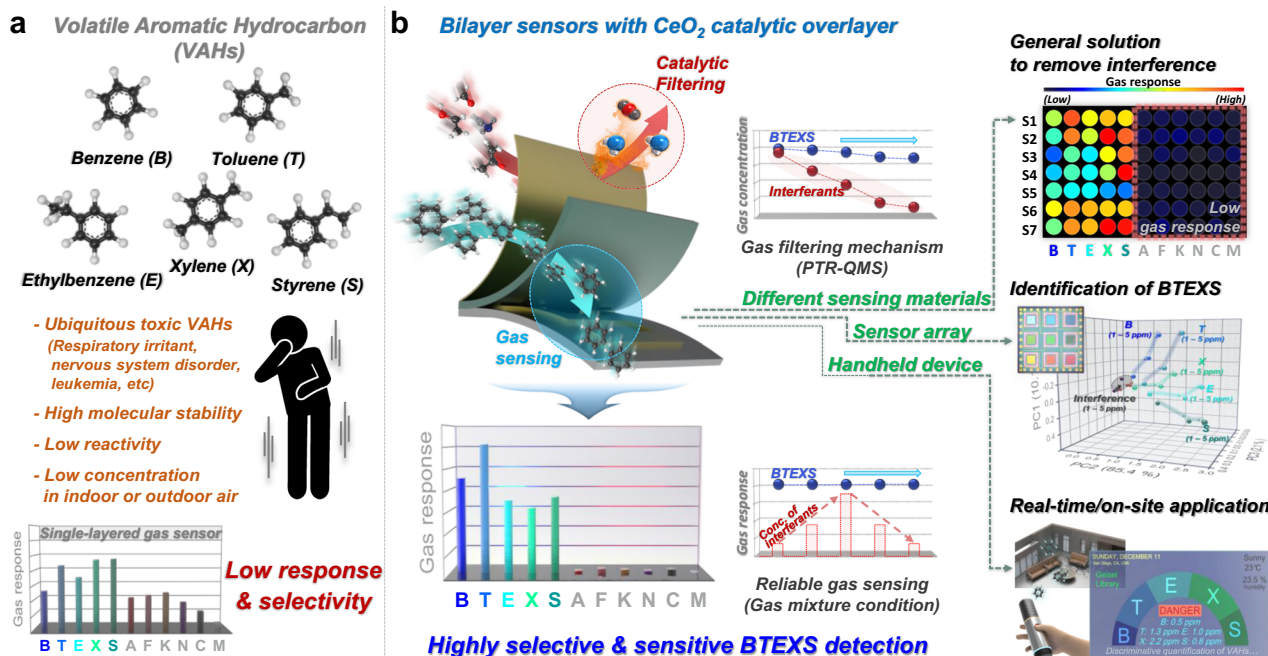


Fig. 1 | Concept of this study. **a** Obstacles for detecting volatile aromatic hydrocarbons (VAHs), i.e., benzene (B), toluene (T), ethylbenzene (E), xylene (X), and styrene (S). **b** Bilayer sensor with catalytic CeO_2 overlayer suggested as a universal

solution for the exclusive detection of VAHs (left) and its potential for various applications (right).

oxygen to induce charge transfer. However, oxide chemiresistive gas sensors often suffer from selective gas detection because the simple gas-sensing mechanism is based on charge transfer between the analyte gas and sensing surface, which becomes more crucial when attempting to detect stable gases such as VAHs. Indeed, most oxide chemiresistors such as SnO_2 , Co_3O_4 , ZnO , TiO_2 , and In_2O_3 exhibit lower gas responses to VAHs than to highly reactive interfering gases such as ethanol, formaldehyde (HCHO), and acetone^{31–34} and often cannot identify or quantify specific chemical species in complex gas mixtures. This problem is related to the molecular stability of aromatic compounds comprising conjugated planar ring systems wherein electrons are strongly delocalized around the rings^{35,36}. To overcome this limitation, although many approaches such as catalyst addition³⁷, nanostucture adoption^{31,38}, heterocomposite implementation³⁹, electronic nose utilization⁴⁰, and preconditioning part application⁴¹ have been explored, their capabilities for discriminating and quantifying aromatic BTEXS remains insufficient for monitoring air quality.

In light of this, assembling catalytic filtering layers (such as Co_3O_4 ⁴², TiO_2 ⁴³, SnO_2 ⁴³, Rh/TiO_2 ⁴⁴, Au ⁴⁵, Pt-loaded Al_2O_3 ⁴⁶, and an external WO_3 packed bed⁴⁷) with gas-sensing films has recently spotlighted as a viable and facile solution for achieving gas selectivity toward aromatic gases by oxidation of the analyte prior to the gas-sensing reaction. Sensors fabricated with catalytic filtering layers are very advantageous because they exhibit highly tunable gas selectivities and responses by independently controlling sensing and catalytic reactions. However, designing sensors with catalytic filtering layers is still in the nascent stage, and high gas-sensing response and selectivity have never been simultaneously achieved toward aromatic BTEXS gases. In addition, sensors should be integrated into portable devices for monitoring air quality on-site and in real-time, which is difficult utilizing external filters such as those used in some previous studies.

Herein, we report a rational and facile strategy for ultraselectively and ultrasensitively detecting traces of aromatic BTEXS gases utilizing a bilayer sensor designed with a catalytic filtering layer (Fig. 1b). The key concept of the bilayer sensor is the catalytic oxidation of highly reactive nonaromatic interferants to less- or non-reactive species prior

to the gas-sensing reaction. Owing to its moderate catalytic activity, CeO_2 was employed as the overlayer material. The main advantage of the bilayer sensor over conventional gas detectors is that cross-responses to highly reactive interfering gases are removed while maintaining high gas responses to aromatic compounds, thereby enabling traces of aromatic BTEXS gases to be discriminated both selectively and quantitatively, even in gas mixtures. The mechanism underlying the exceptional sensing selectivity and the response was systematically studied for the sensing materials, catalytic overlayer, and bilayer structural configuration and validated by monitoring the conversion of analyte gases using a proton transfer reaction-quadrupole mass spectrometer (PTR-QMS). Moreover, the CeO_2 -coated bilayer sensor design was validated by enhancing the BTEXS-sensing properties of diverse gas sensors using SnO_2 , $\text{Pt}-\text{SnO}_2$, $\text{Au}-\text{SnO}_2$, In_2O_3 , $\text{Rh}-\text{In}_2\text{O}_3$, $\text{Au}-\text{In}_2\text{O}_3$, WO_3 , and ZnO . In addition, we demonstrated that a bilayer sensor array with a catalytic CeO_2 overlayer exhibited high or partial selectivity to aromatic compounds but a low gas response to other indoor pollutants to clearly identify BTEXS gases in a highly quantitative and discriminative manner. This study will open various pathways for developing highly precise, reliable, and cost-effective sensors to protect humans from the harmful effects of volatile aromatic compounds.

Results

Fabrication and characterization of gas-sensing films with a catalytic overlayer

A schematic of the monolithic bilayer sensor comprising an $\text{Rh}-\text{SnO}_2$ sensing film and catalytic CeO_2 overlayer is illustrated in Fig. 2a. The $\text{Rh}-\text{SnO}_2$ sensing layer was screen-printed onto an Al_2O_3 substrate (1.5 mm × 1.5 mm) with two Au sensing electrodes (electrode gap: 0.2-mm gap), and the CeO_2 overlayer was coated by electron-beam (e-beam) evaporation. The $\text{Rh}-\text{SnO}_2$ hollow spheres were synthesized by ultrasonic spray pyrolysis and subsequent annealing at 600 °C. Detailed information regarding the sensor fabrication is described in the “Methods” section and Supplementary Note 1. The mean diameter of the ~80 $\text{Rh}-\text{SnO}_2$ spheres was $0.84 \pm 0.37 \mu\text{m}$ (Fig. 2b(i)). The broken

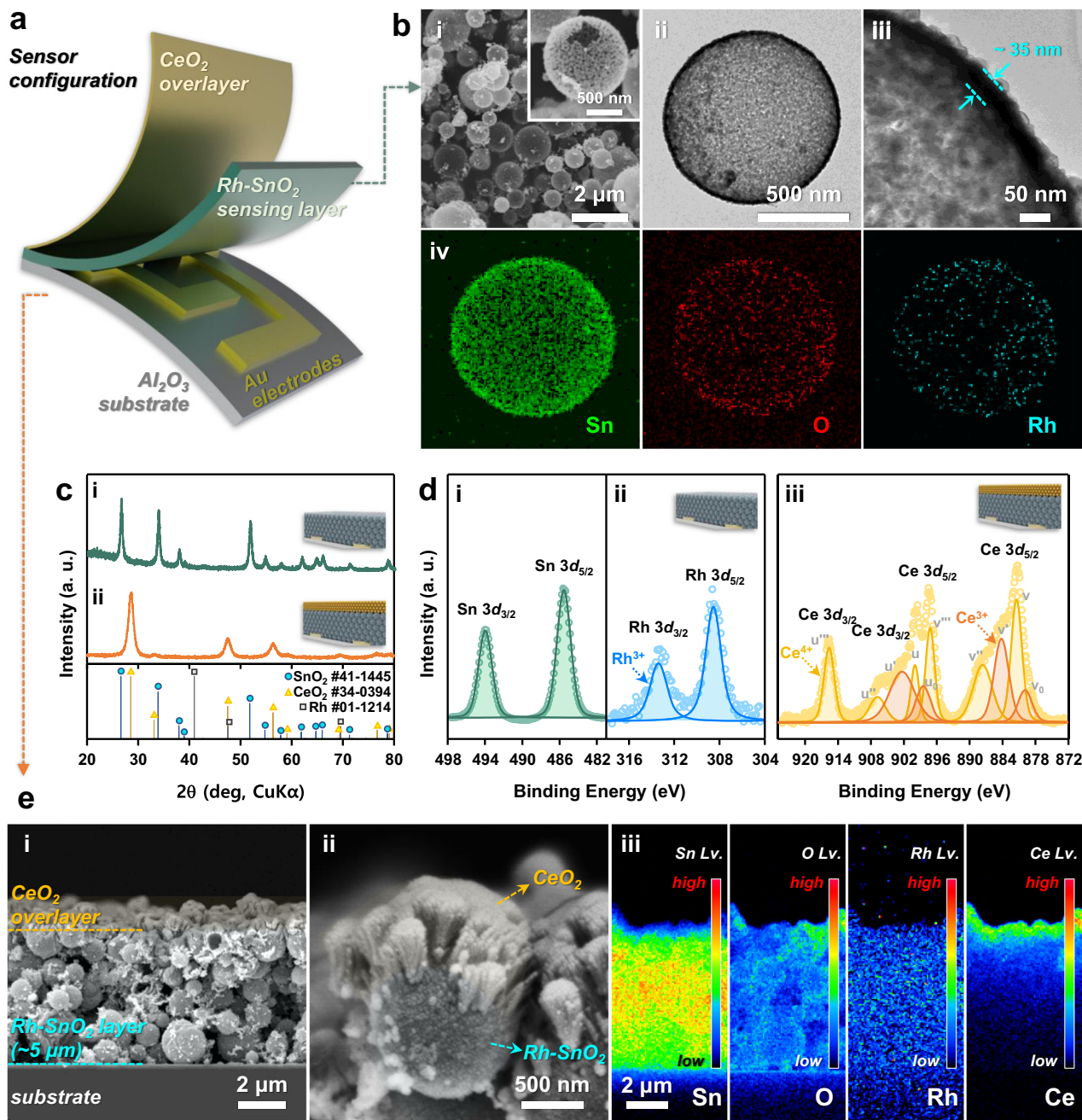


Fig. 2 | Morphology and phase characterizations of Rh-SnO₂ and CeO₂/Rh-SnO₂ sensors. **a** Schematic of CeO₂/Rh-SnO₂ bilayer sensor. **b** Characterization of CeO₂/Rh-SnO₂ bilayer sensor (i) SEM, (ii and iii) TEM, and (iv) EDS elemental (Sn, O, and Rh) mapping images of Rh-SnO₂ powders. **c** XRD patterns of (i) Rh-SnO₂ and (ii) CeO₂/Rh-SnO₂ films. **d** XPS spectrums of the samples.

(i) Sn 3d and (ii) Rh 3d XPS spectra for Rh-SnO₂ film; (ii) Ce 3d XPS spectrum for CeO₂/Rh-SnO₂ film. **e** (i) Cross-sectional SEM, (ii) high-magnification SEM, and (iii) electron-probe microanalysis (EPMA) elemental mapping (Sn, O, Rh, and Ce) images of CeO₂/Rh-SnO₂ film. Source data are provided as a Source Data file.

part of the sphere exhibited a hollow morphology (Fig. 2b(i) inset), which was further confirmed by the bright and dark contours at the central part and outer shell (~35 nm thick) of the spheres, respectively, in the transmission electron microscopy (TEM) images (Fig. 2b(ii), b(iii)). The Brunauer–Emmett–Teller (BET) specific surface area of the Rh-SnO₂ hollow spheres was 35.6 m² g⁻¹, and the N₂ adsorption and desorption isotherms exhibited type IV characteristics with H3 hysteresis loops (Supplementary Fig. 1). These results indicate that the hollow Rh-SnO₂ spherical structure is highly accessible to gases. The tetragonal SnO₂ phase was confirmed by the high-resolution TEM (HR-TEM) image exhibiting lattice patterns with interplanar spacings of 3.31 and 2.69 Å corresponding to the (110) and (101) planes (Supplementary

Fig. 2), respectively, and by the corresponding X-ray diffraction (XRD) patterns (Fig. 2c(i)). No Rh-related phase appeared in the HR-TEM image, nor was indicated by the corresponding XRD pattern probably due to the low detection limit of X-ray diffractometer. However, the energy-dispersive spectroscopy (EDS) elemental mappings revealed that Rh, Sn, and O were uniformly distributed over the entire particle surface (Fig. 2b(iv)). Moreover, a peak corresponding to Rh³⁺ appeared in the X-ray photoelectron spectroscopy (XPS) profile, confirming that Rh was present as Rh₂O₃ (Fig. 2d(ii))^{48,49}.

An ~0.4-μm-thick CeO₂ overlayer was coated on the ~5-μm-thick Rh-SnO₂ gas-sensing film (Fig. 2e(i)), as estimated from the SEM image of the film deposited on the planar SiO₂/Si wafer (Supplementary

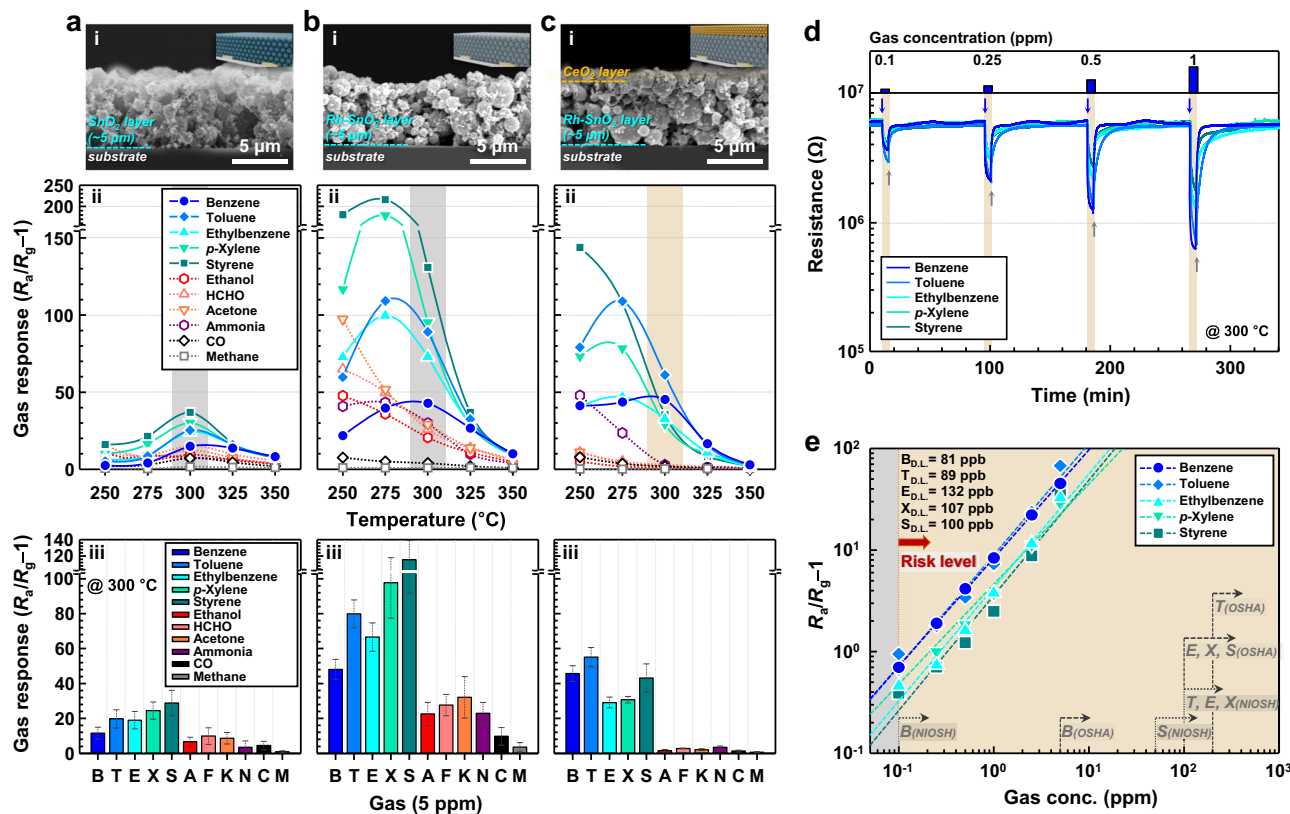


Fig. 3 | Gas-sensing performance of the samples. **a–c** Cross-sectional SEM images and gas-sensing characteristics of SnO_2 (a), Rh-SnO_2 (b), and $0.4\text{CeO}_2/\text{Rh-SnO}_2$ (c) sensors (analyte gas concentration: 5 ppm; error bars indicate standard deviations for three sensors). **d** Dynamic gas-sensing transients of $0.4\text{CeO}_2/\text{Rh-SnO}_2$ sensor exposed to 0.1–1 ppm BTEXS at 300 °C. **e** Gas responses as functions of BTEXS concentration and exposure limits of volatile aromatic compounds based on acute

and chronic inhalation or working conditions (The dashed lines are fitted curves; the linear regression equations are expressed as $y = 0.859x + 1.017$ (B), $y = 0.917x + 1.045$ (T), $y = 0.816x + 0.797$ (E), $y = 0.750x + 0.806$ (X), $y = 0.809x + 0.745$ (S), where y is the gas response and x is the gas concentration). Source data are provided as a Source Data file.

Fig. 3). A high-magnification cross-sectional scanning electron microscopy (SEM) image of the bilayer film uppermost region further shows that the Rh-SnO_2 powder spheres were covered with CeO_2 nanoparticles (Fig. 2e(ii)). Electron-probe microanalysis (EPMA) elemental mapping (Fig. 2e(iii)) revealed that Sn, O, and Rh were distributed throughout the entire film, whereas Ce was only distributed in the top region. The Rh-SnO_2 film with the CeO_2 overlayer was further analyzed using XRD and XPS (Fig. 2c(ii), d(iii) and Supplementary Fig. 4). The CeO_2 overlayer was identified as a cubic fluorite phase (ICDD #34-0394). The Rh-SnO_2 -related peaks disappeared in the XRD pattern and XPS spectrum of the CeO_2 -overlayer-coated Rh-SnO_2 film because of the low detection depth (i.e., few-nanometer depth resolution) of both XRD and XPS (Fig. 2c(ii) and Supplementary Fig. 4).

Exclusive detection of volatile aromatic hydrocarbons using bilayer sensors with a porous Rh-SnO_2 sensing film and a CeO_2 overlayer

The gas-sensing characteristics of the $\text{CeO}_2/\text{Rh-SnO}_2$ bilayer film were measured in the range 250–350 °C for detecting 5 ppm of VAHs (B, T, E, X, and S) and nonaromatic interference gases (ethanol [A], formaldehyde [F], acetone [K], ammonia [N], carbon monoxide [C], and methane [M]) (Fig. 3c). To elucidate the roles of the Rh loading and CeO_2 overlayer, pure ~5-μm-thick SnO_2 and Rh-SnO_2 films, which were similar thickness to that of the Rh-SnO_2 gas-sensing film in the bilayer sensor, were also prepared (Fig. 3a(i), b(i) and Supplementary Fig. 5), and their gas-sensing characteristics were investigated (Fig. 3a(ii), (iii) and b(ii), (iii)). All three sensors exhibited *n*-type oxide semiconductor behavior with decreased resistance in a reducing atmosphere

(Supplementary Fig. 6). Thus, the gas response (S) was defined by Eq. (1) as follows:

$$(R_a - R_g)/R_g = R_a/R_g - 1 \quad (1)$$

where R_a and R_g are the resistances in the air and analyte gas, respectively. See Supplementary Note 1 for the detailed gas-sensing measurements.

The responses to 5 ppm of the various analyte gases are plotted as functions of sensing temperature for the pure SnO_2 sensor (Fig. 3a). Clearly, all the response curves are bell-shaped, and the pure SnO_2 sensor exhibited the highest VAH responses (S_B, S_T, S_E, S_X , and $S_S = 14.9, 25.3, 24.3, 30.2$, and 36.9, respectively) at 300 °C. The aromatic gas responses of SnO_2 sensor were comparable to nonaromatic interfering gases, thereby hindering selective VAH detection. These results are consistent with the typical sensing characteristics of pure SnO_2 reported in the literature^{31,38,50,51}. The Rh-SnO_2 sensor exhibited considerably enhanced gas responses to most of the analyte gases at all the sensing temperatures (Fig. 3b). For example, at 300 °C, the gas responses of the Rh-SnO_2 sensor to 5 ppm of the volatile aromatic hydrocarbons (B, T, E, X, and S) increased to 42.8, 89.1, 73.0, 95.2, and 130.9, respectively, which were ~2.9–3.5-fold higher than those of the pure SnO_2 sensor (Fig. 3b(iii)). The Rh loading-induced increased overall gas response can be explained by the decreased background charge-carrier concentrations caused by the *p*-*n* junction and/or Schottky contact formed between the *n*-type SnO_2 and *p*-type Rh_2O_3 , which work functions are 4.9 and 5.0 eV, respectively^{52–54}, and is supported by the Rh loading increasing the sensor resistance from 0.9 to

2.6 M Ω in the air at 300 °C (Supplementary Fig. 6b). In addition, the chemisorbed oxygen species (O_{ads}^-)/lattice oxygen species (O_{lat}^-) peak ratio for the Rh–SnO₂ sensor was substantially higher than that for the pure SnO₂ sensor (Supplementary Fig. 7), indicating that Rh-induced oxygen spillover was also responsible for the increased response. Notably, the gas responses of the Rh–SnO₂ sensor were considerably higher than the Pd–SnO₂, Pt–SnO₂, and Au–SnO₂ sensor counterparts (Supplementary Note 2 and Supplementary Figs. 8, 9), indicating that among the noble-metal catalysts, Rh was the most effective for promoting VAH sensing. However, because loading of Rh to SnO₂ enhanced responses to not only VAHs but also nonaromatic interference gases (Fig. 3b), the Rh–SnO₂ sensor was still insufficient for selectively detecting VAHs.

In contrast, coating a 0.4-μm-thick CeO₂ overlayer on the Rh–SnO₂ film surface (hereafter, 0.4CeO₂/Rh–SnO₂) considerably decreased the interfering-gas responses, whereas the VAH responses remained high (Fig. 3c). It is worth noting that the 0.4CeO₂/Rh–SnO₂ sensor selectively and sensitively detected VAHs over a wide sensing-temperature range (275–350 °C). In particular, the sensor exhibited remarkably high gas responses of S_B , S_T , S_E , S_X , and S_S = 45.3, 61.2, 32.7, 29.2, and 35.4, respectively, to 5 ppm VAHs and negligible interfering-gas cross-responses of S_A , S_F , S_K , S_N , S_C , and S_M = 1.0, 3.0, 2.1, 2.9, 1.9, and 0.3, respectively, at 300 °C, thereby demonstrating exclusive aromatic hydrocarbon detection. To investigate the catalytic CeO₂ overlayer thickness effect on VAH detection, Rh–SnO₂ sensors were fabricated with different CeO₂ overlayer thicknesses: 0.05CeO₂/Rh–SnO₂, 0.1CeO₂/Rh–SnO₂, and 0.7CeO₂/Rh–SnO₂ (Supplementary Figs. 10, 11). All the sensors selectively and sensitively detected VAHs over a wide temperature range (Supplementary Figs. 11, 12 and Supplementary Note 3), clearly indicating that coating the gas-sensing film with a CeO₂ overlayer is a promising strategy for exclusively detecting VAHs. At 300 °C, because the 0.4CeO₂/Rh–SnO₂ sensor exhibited the highest VAH selectivity (e.g., VAH selectivity increased with increasing CeO₂ coating thickness to 0.4 μm and subsequently decreased with further increasing CeO₂ coating thickness from 0.4 to 0.7 μm) (Supplementary Fig. 12), the optimal CeO₂ overlayer thickness and operating temperature of the bilayer sensor were fixed at 0.4 μm and 300 °C, respectively. In addition, a similar tendency in gas responses was further achieved from each sensor batch (Supplementary Fig. 13), which confirms the excellent sensor reproducibility.

To demonstrate the potential of 0.4CeO₂/Rh–SnO₂ as an indoor air-monitoring sensor, the cyclic sensing characteristics to 0.1–1 ppm of aromatic hydrocarbons (BTEXS) were examined at 300 °C (Fig. 3d). Moreover, from the graph of the gas response plotted as a function of the gas concentration, the detection limit (DLs) of aromatic hydrocarbons were calculated using the sensing criterion $R_a/R_g - 1 > 0.2$ as 81 ppb (B), 89 ppb (T), 132 ppb (E), 107 ppb (X), and 100 ppb (S), respectively (Fig. 3e)^{55,56}. The low detection limits of 0.4CeO₂/Rh–SnO₂ sensor were further estimated to be 16 ppb (B), 62 ppb (T), 114 ppb (E), 75 ppb (X), and 52 ppb (S) when $3(RMS_{noise}/Slope)$ was used as the criterion for gas sensing⁵⁷ or 0.017 ppb (B), 0.019 ppb (T), 0.020 ppb (E), 0.014 ppb (X), and 0.037 ppb (B) when a signal-to-noise ratio > 5 was used as the sensing criterion^{30,58}, respectively (Fig. 3e). All the theoretical detection limits were considerably lower than the permissible exposure limits for the 8 h time-weighted average (TWA) established by the National Institute for Occupational Safety and Health (NIOSH) and Occupational Safety and Health Administration (OSHA)^{59–63}, indicating that the 0.4CeO₂/Rh–SnO₂ sensor can be used to accurately monitor sub-ppb levels of hazardous aromatic hydrocarbons. Furthermore, the stability of the 0.4CeO₂/Rh–SnO₂ bilayer sensor was verified by reproducing sensing properties during seven consecutive cycles and long-term cycling for 24 days (Supplementary Fig. 14).

The ambient humidity effect of the 0.4CeO₂/Rh–SnO₂ sensor, which is important for their practical applications such as indoor air

quality monitoring, was also investigated by measuring gas sensing characteristics under simulated indoor conditions (static atmosphere; relative humidity (RH) 50%; temperature 18 °C) (Supplementary Fig. 15). For this, the relative humidity of an acrylic chamber (inner volume: 50 cm × 50 cm × 50 cm) was controlled by a humidifier and the analyte gases were filled into the chamber by evaporating the high-purity solutions (benzene, toluene, ethylbenzene, *p*-xylene, styrene, and ethanol). The final concentrations of analytes were fixed at 5 ppm. The detailed measurement was conducted using the following procedures: when the sensor resistance was constant, the sensor was injected into the chamber and the variation of sensor resistance was measured for 100 s, subsequently recovered to its original resistance via ejecting the sensor from the chamber. The 0.4CeO₂/Rh–SnO₂ sensor exhibited high selectivity toward VAHs over ethanol (S_B/S_A = 1.4, S_T/S_A = 5.5, S_E/S_A = 5.8, S_X/S_A = 5.1, and S_S/S_A = 3.5, respectively) under the simulated conditions (RH 50%) (Supplementary Fig. 15b). Although the decrease of sensor response was observed in the simulated atmosphere, the gas selectivity toward VAHs remained substantial. These results demonstrate that the fabricated sensor can be used to detect sub-ppm-level VAHs in a real environment.

Exceptional high performance in gas mixtures

Under actual gas-sensing conditions, volatile aromatic compounds (BTEXS) coexist with different concentrations of airborne chemicals, which often hinders quantifying gas concentrations^{1,2,12,64}. To determine the reliable sensing under interferant, the sensor responses to 5 ppm of pure B, T, E, X, or S and the same in mixed gases were measured at 300 °C by varying the interfering-gas type and concentration i.e., 0.1–5 ppm of ethanol, HCHO, or acetone (Fig. 4, Supplementary Fig. 16, and Supplementary Note 4). For the Rh–SnO₂ sensor, the gas responses to 5 ppm of B, T, E, X, or S varied considerably depending on the interfering-gas concentration in the gas mixture (i.e., the B, T, E, X, and S responses showed average variations of 21.3, 15.0, 17.6, 13.0, and 12.0%, respectively, as shown in Fig. 4a and Supplementary Fig. 16b, d). In stark contrast, the 0.4CeO₂/Rh–SnO₂ sensor exhibited nearly identical B, T, E, X, or S gas responses, regardless of the interfering gas (i.e., the B, T, E, X, and S responses showed average variations of 5.1, 2.7, 2.7, 3.7, and 4.0%, respectively, under the same experimental conditions, as shown in Fig. 4b and Supplementary Fig. 16c, e). This result confirms the exceptional selectivity for aromatic hydrocarbons in gas mixtures, which originates from the distinctive bilayer design with a catalytic CeO₂ overlayer.

Gas-sensing mechanism and catalytic characterization

Notably, exclusively detecting aromatic hydrocarbons with negligible cross-responses to nonaromatic interference gases can hardly be achieved using common single-layered gas sensors (e.g., gas-sensing films comprising uniformly doped/loaded noble-metal or oxide catalysts and nanostructured building blocks)^{31,37–39,52–54}. This is supported by the relatively low gas response and selectivity of the common single-layered sensors such as Au-loaded hierarchical MoO₃ hollow spheres³⁷, CuO nanoparticles⁵⁹, CuO/SnO₂ composites⁵⁰, SnO₂/V₂O₅ composites⁵¹, Hexagonal WO₃ nanosheets⁵², Triangular-CeO₂-nanoflake-coated ZnO sensor⁵³, Cr-doped Co₃O₄ nanorods⁵⁴, Pd-decorated SnO₂ nanowires⁵⁵ (Fig. 5). However, both high gas responses (S_{VAH}) and excellent selectivities (S_{VAH}/S_A) toward aromatic BTEXSs were simultaneously achieved using monolithic bilayer sensors with a catalytic CeO₂ overlayer, and are the highest values among those reported in the literature (Fig. 5 and Supplementary Table 1)^{37,42–45,59–52,23}. The intriguing gas-sensing characteristics of the bilayer sensor can be explained by gas filtering through the CeO₂ catalytic overlayer because the gas-sensing layer (bottom) and catalytic overlayer (top) were completely separated. In the bilayer sensor structure, the analyte gases were transported to the bottom sensing electrodes through the top CeO₂ overlayer, and the bottom Rh–SnO₂ film was mainly responsible

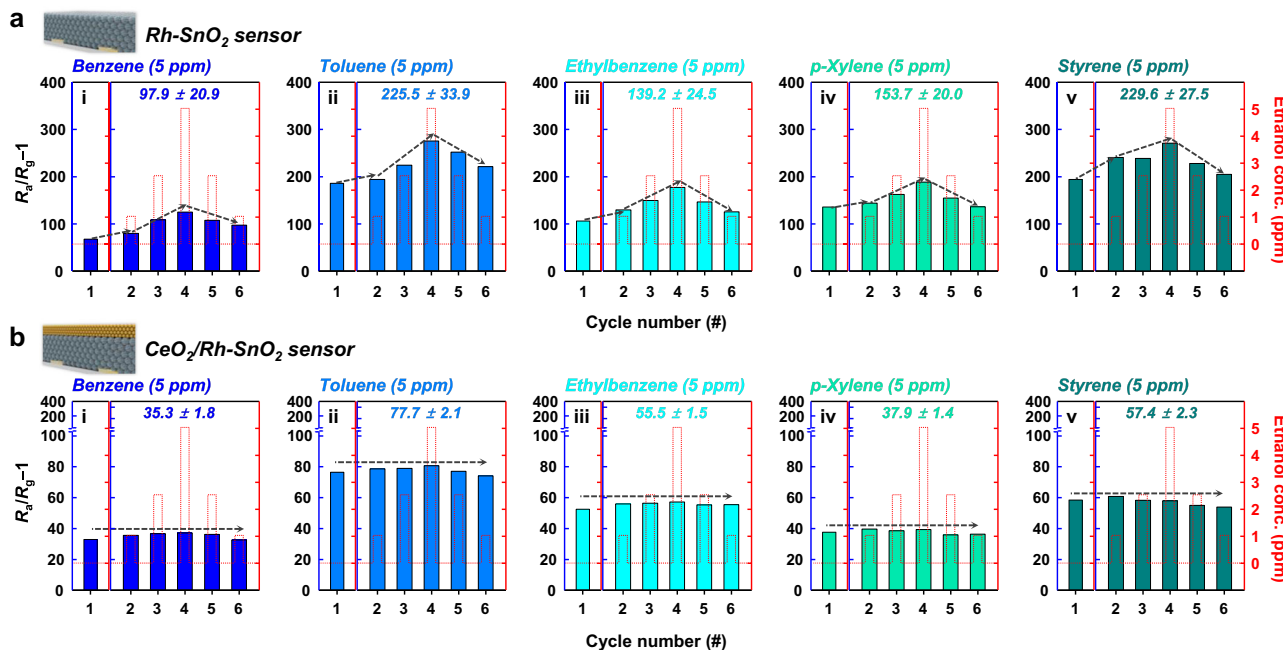


Fig. 4 | Multi-component gas-sensing analysis. **a, b** Gas responses of the Rh-SnO₂ (a) and the 0.4CeO₂/Rh-SnO₂ (b) sensors to (i) gas mixture of 5 ppm benzene (filled bars) and 0–5 ppm ethanol (dashed red lines), (ii) gas mixture of 5 ppm toluene (filled bars) and 0–5 ppm ethanol (dashed red lines), (iii) gas mixture of 5 ppm ethylbenzene (filled bars) and 0–5 ppm ethanol (dashed red lines), (iv) gas mixture of 5 ppm *p*-xylene (filled bars) and 0–5 ppm ethanol (dashed red lines), and (v) gas

mixture of 5 ppm styrene (filled bars) and 0–5 ppm ethanol (dashed red lines) at 300 °C. Note that the Rh-SnO₂ sensor showed a concentration-dependent response variations toward ethanol, while the response of the 0.4CeO₂/Rh-SnO₂ sensor was barely affected by the coexistence of 0–5 ppm of ethanol. Source data are provided as a Source Data file.

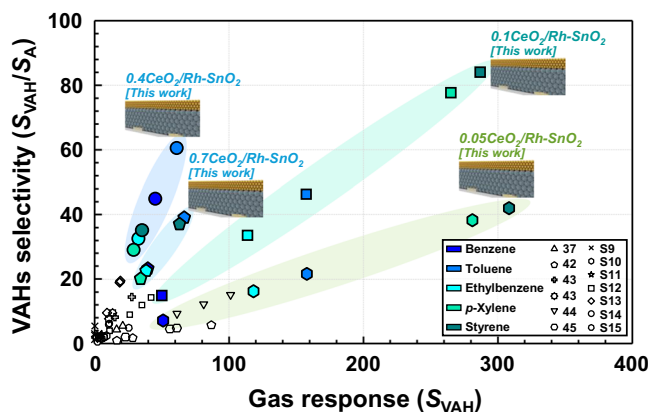
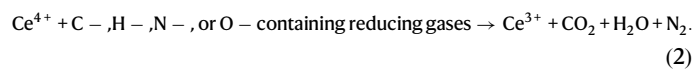


Fig. 5 | Gas-sensing performance of CeO₂/Rh-SnO₂ bilayer sensors. Selectivities ($S_{VAH}/S_{ethanol}$) and responses (S_B , S_T , S_E , S_X , and S_S) to VAHs measured in this study compared to those previously reported in the literature^{37,42–45,59–62}. Source data are provided as a Source Data file.

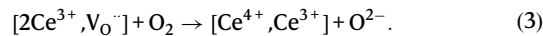
for the gas-sensing reaction. Thus, the top CeO₂ layer transformed the analyte gases into less- or non-reactive forms through catalytic oxidation, which explains why the gas response decreased when the Rh-SnO₂ film was coated with the CeO₂ overlayer.

Accordingly, the gas responses to both VAHs and other representative interfering gases (e.g., ethanol, formaldehyde, and acetone) were plotted as functions of the CeO₂ layer thickness (Supplementary Fig. 17). At all the sensing temperatures (250–350 °C), the gas responses to both the VAHs and interfering gases gradually decreased with increasing CeO₂ overlayer thickness. Despite nearly the same Rh-SnO₂-sensing-film thickness being employed, the decreased gas response suggests that the gases were oxidatively consumed at the CeO₂ overlayer, which is plausible because CeO₂ exhibits Ce³⁺ and Ce⁴⁺

multivalencies and abundant oxygen vacancies and, therefore, excellent thermocatalytic activity for oxidizing reducing gases⁶⁵. Notably, Ce⁴⁺ interacts with C-, H-, N-, or O-atom-containing reducing gases and is reduced to Ce³⁺, thereby oxidizing the reducing gas to less- or non-reactive forms (e.g., CO₂, H₂O, or N₂) through Reaction (2) as follows^{66,67}:



In addition, the CeO₂ oxygen vacancies promote oxygen adsorption, which facilitates reducing gas oxidation through Reaction (3) as follows^{66,67}:



To determine whether multivalencies and oxygen vacancies, which might be affected by gas oxidation, formed in the CeO₂, XPS, and electron paramagnetic resonance (EPR) analysis were carried out and shown in Fig. 2d(iii) and Supplementary Fig. 18, respectively. As demonstrated in the XPS measurement (Fig. 2d(iii)), the coexistence of Ce³⁺ and Ce⁴⁺ in CeO₂ was confirmed by Ce 3d spectra observation. Furthermore, the EPR spectrum exhibited a peak at $g \approx 1.960$, indicating that the CeO₂ also exhibited oxygen vacancies (Supplementary Fig. 18)⁶⁸.

However, these results cannot elucidate the remarkably high selectivity of the CeO₂/Rh-SnO₂ sensors toward aromatic compounds, and the chemiresistive variation induced by CeO₂ depends on the gas species. Considering that aromatic compounds with benzene ring are known to be very stable whereas the non-volatile aromatic compounds gases are more reactive than VAHs³⁶, the highly selective VAH detection can be associated with the complete oxidation of highly reactive nonaromatic gases and survival of less reactive BTEX gases during transport across the CeO₂ overlayer. This is supported by the fact that,

the responses to aromatic BTEXS gases decreased slightly, whereas those to nonaromatic gases decreases down to negligible levels, as shown in Fig. 3b, c, respectively, thereby leading to selective and sensitive VAH detection.

The sensor temperature required to achieve the maximum gas response (T_M) also supports the proposed mechanism. Oxide chemiresistor response curves plotted as functions of sensing temperature are usually bell-shaped^{12,69,70}. For instance, in the low-sensing-temperature region, the gas response gradually increased through the thermal promotion of the sensing reaction between the analyte gas and ionized surface O atoms. At excessively high sensing temperatures, the gas response decreased because the analyte gases were oxidized to nonreactive species (e.g., CO₂ or H₂O) at the upper part of the gas-sensing film before diffusing to the bottom sensing region near the electrodes. Since the gas-sensing reactions of more-reactive gases (e.g., ethanol, HCHO, and acetone) can be promoted at lower temperatures, the higher gas reactivity reduces T_M . Notably, the T_M values for benzene and the other aromatic TEXs gases were 300 and 275 °C, respectively, which are considerably higher than those of other non-aromatic gases ($T_M \leq 250$ °C) (Fig. 3b(ii)). This indicates that the catalytic CeO₂ layer can selectively remove highly reactive nonaromatic gases at moderate sensing temperatures (e.g., 300 and 275 °C) without expending VAHs because the oxidative consumption of highly reactive interfering gases begins at a relatively low temperature (≤ 250 °C) (Fig. 3b(iii)).

The effects of the CeO₂ overlayer thickness on the gas sensing characteristics are also important for understanding the oxidative consumption of interfering gases. The single-layer Rh-SnO₂ sensor exhibited high and comparable responses to a wide range of reducing gases. In contrast, all four sensors coated with 0.05-, 0.1-, 0.4-, and 0.7-μm-thick CeO₂ overlayers showed high gas selectivity and response to VAHs, confirming the interfering gases were successfully filtered by catalytic oxidation in the CeO₂ overlayer. For example, the thin (0.05- and 0.1-μm-thick) CeO₂ overlayers led to relatively high cross-responses to interfering gases, probably due to insufficient oxidation of interfering gases, resulting in low selectivity to VAHs (Supplementary Figs. 12 and 13). However, excessive thickening of (0.7-μm-thick) CeO₂ overlayer significantly reduced the gas responses to both VAHs and interfering gases (Supplementary Figs. 11c, f and 13f), and this could be related to the catalytic oxidation of all analyte gases, including the VAHs. All these explanations support that the CeO₂ overlayer coatings are effective for oxidative filtering of interfering gases, but the careful control of the CeO₂ overlayer thickness could be crucial for achieving high selectivity and response to VAHs.

To elucidate the gas-sensing mechanism, the catalytic activity of CeO₂ nanoparticles was investigated by converting (η) 1 ppm of benzene, toluene, ethylbenzene, *p*-xylene, and styrene as well as interfering ethanol and HCHO using a PTR-QMS (Fig. 6, Supplementary Note 5, and Supplementary Fig. 19). For this, 0.1 g of CeO₂ nanoparticles were loaded onto quartz wool in the middle of a furnace. The interference gases (ethanol and HCHO) were completely removed below 100 °C, whereas the VAH conversion was low (loss ratio $\approx 0\%$) (Fig. 6). The VAH catalytic conversions were gradually promoted by increasing the temperature because stable aromatic compounds catalytically oxidize more predominantly at high temperatures^{12,63,64,71,72}. Interestingly, in the range 250–350 °C, the VAHs with high molecular stability were not fully oxidized by the CeO₂ catalyst (Fig. 6 and Supplementary Fig. 19c), and the conversion ratio was also different depending on the reactivity of the aromatic compounds, which can enable the gas selectivity and response toward aromatic compounds to be tailored and controlled systematically. These findings clearly suggest that the interfering gases were filtered through oxidative consumption without expending any aromatic BTEXS gases at the catalytic CeO₂ overlayer, which enabled the exclusively high selectivity and response to volatile aromatic compounds and highlights the

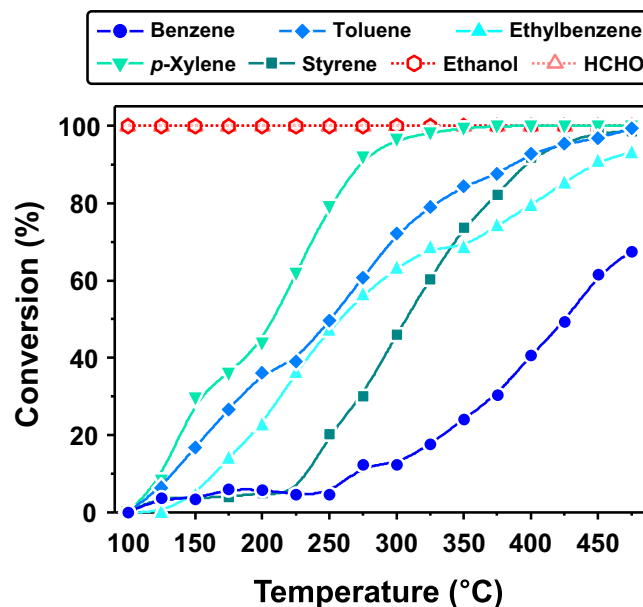


Fig. 6 | Catalytic performance of CeO₂. Catalytic conversion of 5 ppm of different analyte gases over CeO₂ catalyst as functions of temperature in the range 100–475 °C. Source data are provided as a Source Data file.

advantages of the proposed bilayer structure fabricated with the CeO₂ overlayer.

Universal sensor design for detecting volatile aromatic hydrocarbons

The general validity for designing sensors with a CeO₂ overlayer was investigated using different sensing materials (Figs. 7, 8 and Supplementary Fig. 20). The diverse gas sensing materials were also prepared via ultrasonic spray pyrolysis (Supplementary Note 6). The gas-detecting characteristics are summarized in Supplementary Fig. 21, and the normalized responses are displayed in different colors according to the scale bar to facilitate comparison (Fig. 7a, b). The gas responses of the single-layer sensors (SnO₂, Pt-SnO₂, Au-SnO₂, In₂O₃, Rh-In₂O₃, Au-In₂O₃, WO₃, and ZnO) to the aromatic BTEXS were comparable to or slightly higher than those of the same sensors to the other gases over the entire operating-temperature range (Figs. 7a and 8a(i)–h(i), and Supplementary Fig. 21a(i)–h(i), a(ii)–h(ii)). The incomparable differences in the gas responses support again that exclusively detecting low-reactivity VAHs is difficult using a simple sensor design like those previously reported in the literature^{22,33,37,42–44,51,73–78,89–92}. However, the coating and increase of the CeO₂ overlayer thickness to 0.05, 0.1, and 0.4 μm reduced the gas response to the interfering gases, confirming the excellent batch-to-batch reproducibility. In particular, when the sensing layer was completely coated with an ~0.4-μm-thick CeO₂ overlayer, although the responses to the nonaromatic interference gases significantly decreased over a wide temperature range, the responses to most of the BTEXS gases remained high, thereby enabling highly selective and sensitive VAH detection (Figs. 7b and 8a(ii)–h(ii), and Supplementary Fig. 21a(i)–h(i), a(iii)–h(iii)). Indeed, the CeO₂-coated sensors exhibited considerably increased selectivities to aromatic BTEXS gases: 5.5 (0.4CeO₂/SnO₂ at 300 °C), 4.0 (0.4CeO₂/Pt-SnO₂ at 275 °C), 6.9 (0.4CeO₂/Au-SnO₂ at 300 °C), 3.2 (0.4CeO₂/In₂O₃ at 350 °C), 5.9 (0.4CeO₂/Rh-In₂O₃ at 375 °C), 4.7 (0.4CeO₂/Au-In₂O₃ at 375 °C), 8.7 (0.4CeO₂/WO₃ at 275 °C), and 5.1 (0.4CeO₂/ZnO at 325 °C) compared to the selectivities of the single-layer sensors

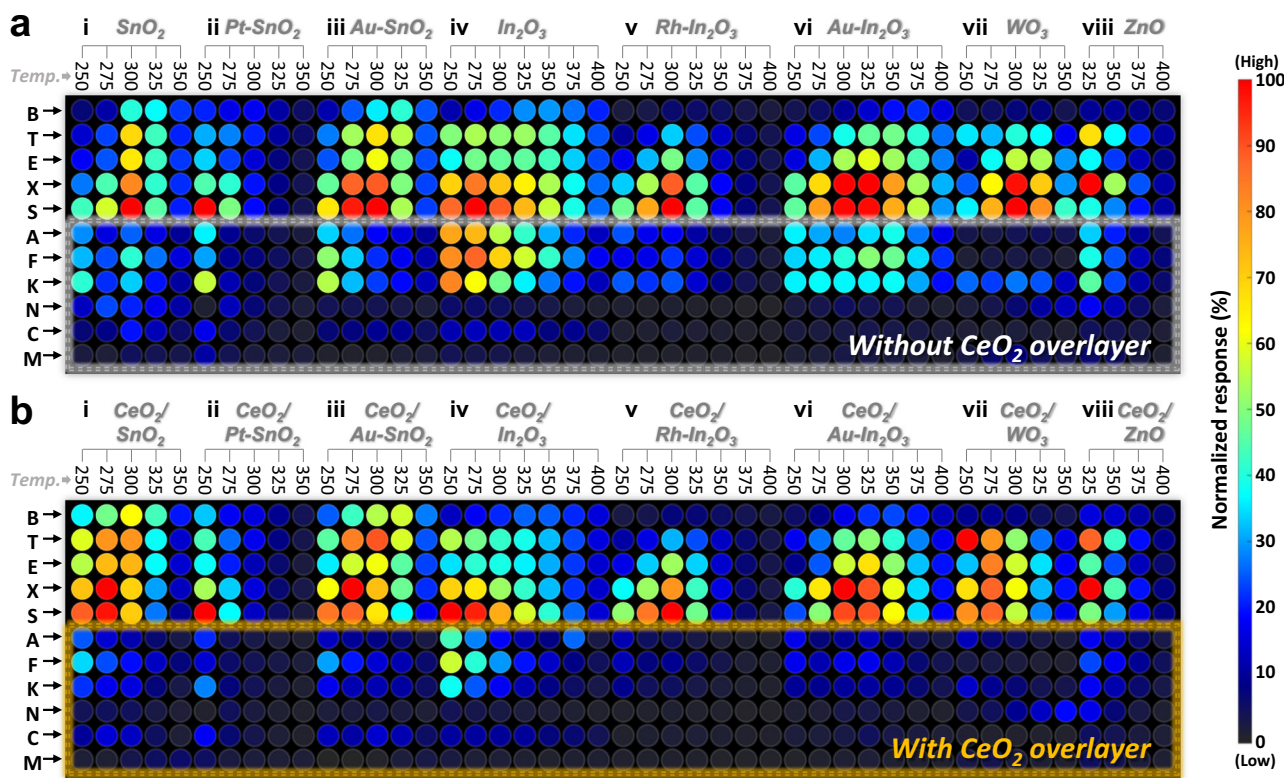


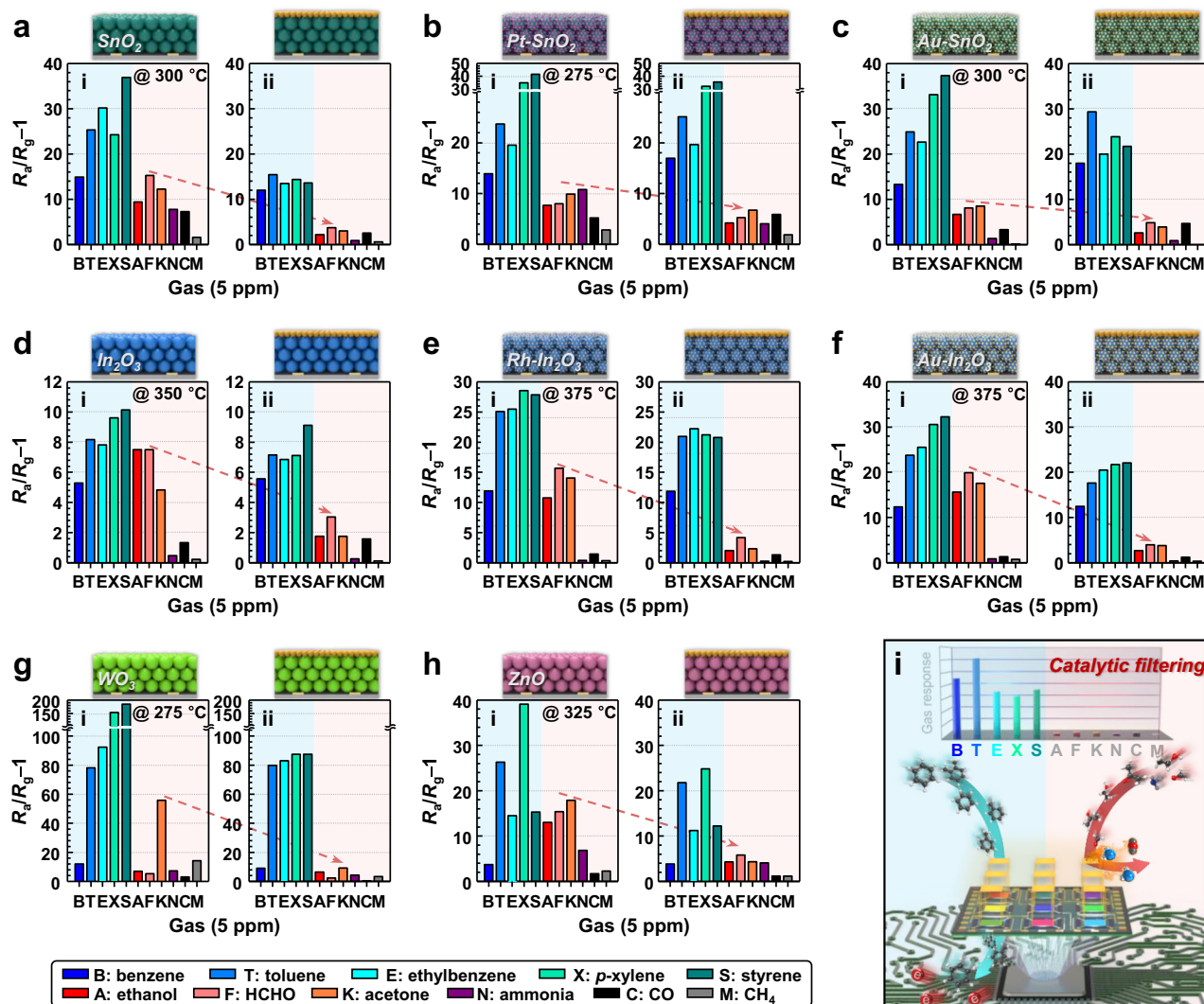
Fig. 7 | Gas-sensing patterns for diverse sensors. **a**, **b** Normalized signal intensities of diverse single-layer sensors (**a**; (i) SnO₂, (ii) Pt-SnO₂, (iii) Au-SnO₂, (iv) In₂O₃, (v) Rh-In₂O₃, (vi) Au-In₂O₃, (vii) WO₃, and (viii) ZnO) and CeO₂-coated bilayer sensors (**b**; (i) 0.4CeO₂/SnO₂, (ii) 0.4CeO₂/Pt-SnO₂, (iii) 0.4CeO₂/Au-SnO₂, (iv) 0.4CeO₂/

fabricated without a CeO₂ overlayer. These results confirm that the CeO₂ overlayer can be applied to diverse sensing materials to achieve exceptional VAH selectivity by suppressing cross-responses to nonaromatic gases through oxidative filtering (Fig. 8i). Notably, not only the R_a values but also the responding (τ_{res}) and recovering (τ_{recov}) kinetics of the bilayer sensors were similar to those of the single-layer sensors (Supplementary Figs. 22 and 23, respectively), which enabled the gas response and selectivity to be controlled without altering the intrinsic sensor resistance and rapid sensing capability (Supplementary Note 7 and 8). Furthermore, the validity of the CeO₂ overlayer coating on Rh-SnO₂ sensors with different morphology (hierarchically porous Rh-SnO₂ and Rh-SnO₂ nanoparticles) was also evaluated (Supplementary Figs. 24). Overall, the CeO₂-coated Rh-SnO₂ with different morphologies showed high selectivity toward VAHs, indicating the coating of CeO₂ overlayer can be applied to variable structured sensing materials. In this respect, these distinctive features of bilayer sensors originating from effectively separating the sensing and catalytic reactions can provide a universal and facile solution for tailoring the gas-sensing characteristics of aromatic compounds.

The quantitative and discriminative detection of volatile aromatic compounds using bilayer sensor arrays

More importantly, the gas selectivities between the BTEX gases could be further tuned in the bilayer sensor designs. For instance, by changing the overlayer thickness, operating temperature, and sensing material, different partial selectivities to specific aromatic gases and negligible cross-responses to interfering gases were achieved using diverse oxide chemiresistors fabricated with CeO₂ overlayers (Fig. 9a). Because these distinctive gas selectivities can be used to discriminate

different aromatic BTEX gases, 3 × 3 multisensor arrays were assembled utilizing the 0.05CeO₂/Rh-SnO₂, 0.1CeO₂/Rh-SnO₂, 0.4CeO₂/Rh-SnO₂, 0.7CeO₂/Rh-SnO₂, 0.4CeO₂/Au-SnO₂, 0.4CeO₂/Rh-In₂O₃, 0.4CeO₂/Au-In₂O₃, 0.4CeO₂/WO₃, and 0.4CeO₂/ZnO sensors, and principal component analysis (PCA) was employed to demonstrate the BTEX gas discrimination capability (Fig. 9b and Supplementary Note 9). Interestingly, the PCA results revealed that the aromatic BTEX were clearly separated from the nonaromatic ones and classified into five nonoverlapping clusters, even at various gas concentrations (e.g., 1, 2.5, and 5 ppm), indicating that the aromatic gases could be discriminated. To investigate the contribution of each sensor to the PCA result, we compared the PCA results by subtracting one of the nine sensors (Supplementary Fig. 25). Similar patterns with PCA plot generated from the nine sensors array were obtained even subtracting sensor (i), (ii), (v), (vii), or (ix). However, the quantitative discrimination of VAHs cannot be achieved by subtracting sensor (iii) 0.4CeO₂/Rh-SnO₂, (iv) 0.7CeO₂/Rh-SnO₂, or (vi) 0.4CeO₂/Rh-In₂O₃, indicating that the contribution of the three sensors' sensing pattern is dominant for determining the PCA results for quantitative and discriminative detection of volatile aromatic compounds (Supplementary Fig. 25c, d, f). Thus, the PCA plot similar to the sensor array consisting of nine sensors could be achieved by conducting PCA using the three major sensors (Fig. 9c). This finding has important implications because the sensors and sensor array can provide comprehensive information (e.g., gas composition and concentration) for precise and economical monitoring of aromatic gases. This finding has important implications for monitoring the health impact of aromatic gases. Moreover, the results of this study suggest that the CeO₂-overlayer-coated sensors and sensor array are versatile, facile, and promising platforms for exclusively detecting aromatic BTEX.

**Fig. 8 | Gas responses for diverse sensors at optimal operation temperature.**

a–h Response properties of diverse (i) single-layer sensors and (ii) CeO₂-coated bilayer sensors (sensing layer material: SnO₂ (a), Pt-SnO₂ (b), Au-SnO₂ (c), In₂O₃

(d), Rh-In₂O₃ (e), Au-In₂O₃ (f), WO₃ (g), and ZnO (h)). **i** Schematic showing the detection mechanism of the bilayer sensor. Source data are provided as a Source Data file.

Discussion

In the present study, we proposed an effective strategy for highly selectively and sensitively detecting traces (on the order of ppb) of volatile aromatic compounds without any interference from other indoor air pollutants. For this purpose, bilayer sensors with catalytic CeO₂ overlayer were designed as a promising and facile sensor platform for tailoring gas-sensing characteristics. The CeO₂-overlayer-coated Rh-SnO₂ sensors exhibited high selectivity and responses to aromatic BTEXS, which enabled these gases to be discriminated, even in gas mixtures. PTR-QMS analysis revealed that this exceptional VAH sensing capability was attributed to the catalytic oxidation of highly reactive interfering gases to less- or nonreactive forms by the CeO₂ overlayer, which exhibited moderate catalytic activity. Furthermore, we demonstrated the general validity of the bilayer sensor design concept by coating a CeO₂ overlayer on the diverse sensing film using SnO₂, Pt-SnO₂, Au-SnO₂, In₂O₃, Rh-In₂O₃, Au-In₂O₃, WO₃, and ZnO. In addition, pattern recognition using the nine-sensor array clearly distinguished between aromatic and nonaromatic gases and quantitatively identified aromatic BTEXS. The findings of this study should lead to opportunities for designing highly precise, reliable, and cost-effective personal sensors for monitoring indoor and outdoor air qualities.

Methods

Synthesis of sensing materials

Rh-loaded SnO₂ (Rh-SnO₂) hollow spheres were synthesized using ultrasonic spray pyrolysis and subsequent calcination. Tin(II) chloride dihydrate (6.7698 g, 0.1 M), rhodium(III) chloride hydrate (0.0315 g, 0.5 at%), citric acid monohydrate (15.9197 g, 0.25 M), and diluted hydrochloric acid solution (35.0–37.0%, 6 mL) were dissolved in 300 mL of distilled water, and the solution was stirred for 1 h at room temperature (23 °C). A clear solution containing uniformly distributed Rh and Sn salts was sprayed using six ultrasonic transducers (resonance frequency: 1.7 MHz), and the droplets were transported in a carrier air gas (flow rate: 20 L min⁻¹) to a high-temperature quartz reactor (700 °C). The spray pyrolysis system used in this experiment is shown in Supplementary Fig. 26a. The Rh- and Sn-containing precursor powders were both collected and annealed at 600 °C for 3 h to remove the residual carbon components and convert the powders into Rh-SnO₂ spheres. For comparison, pure hollow SnO₂ spheres were also synthesized using ultrasonic spray pyrolysis from an Rh-free solution. The experimental procedures for preparing the other gas-sensing materials (Pd-SnO₂, Pt-SnO₂, Au-SnO₂, In₂O₃, Rh-In₂O₃, Au-In₂O₃, WO₃, and ZnO hollow spheres) are described in the Supporting Information.

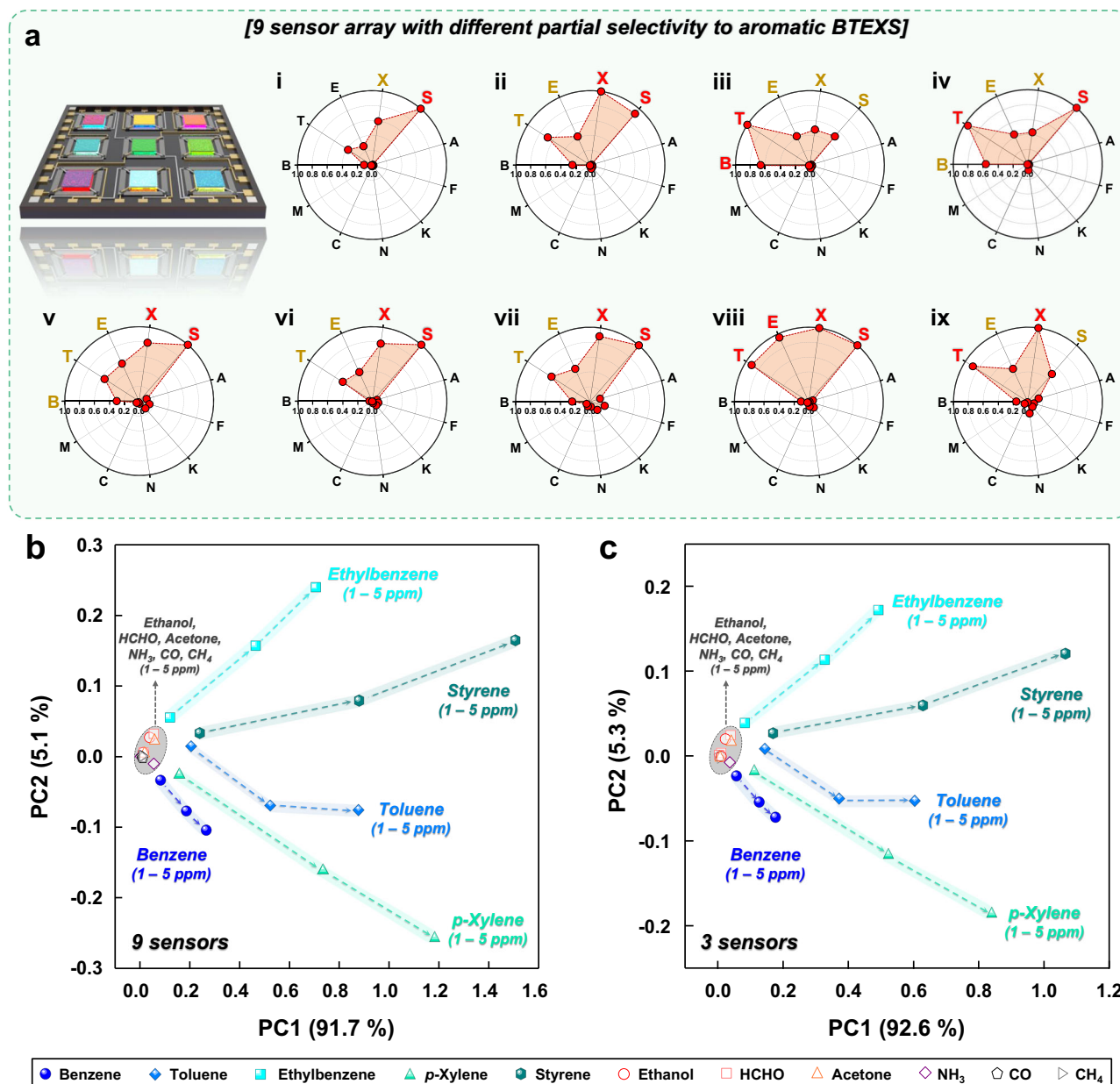


Fig. 9 | Quantitative and discriminative detection of volatile aromatic compounds using bilayer sensor arrays. **a** Polar plots of responses to 5 ppm of analyte gases for (i) 0.05CeO₂/Rh-SnO₂, (ii) 0.1CeO₂/Rh-SnO₂, (iii) 0.4CeO₂/Rh-SnO₂, (iv) 0.7CeO₂/Rh-SnO₂, (v) 0.4CeO₂/Au-SnO₂, (vi) 0.4CeO₂/Rh-In₂O₃, (vii) 0.4CeO₂/Au-In₂O₃, (viii) 0.4CeO₂/WO₃, and (ix) 0.4CeO₂/ZnO sensors (B: benzene, T: toluene, E: ethylbenzene, X: p-xylene, S: styrene, A: ethanol, F: HCHO, K: acetone, N: ammonia, C: CO, and M: CH₄). **b** PCA plot generated using data obtained from a 3 × 3 sensor array exhibiting different partial selectivities to demonstrate aromatic BTEX gas discrimination over the interferences from ethanol, HCHO, acetone, ammonia, CO, and CH₄ (concentrations: 1–5 ppm). **c** PCA result constructed by data obtained from three major sensors ((iii) 0.4CeO₂/Rh-SnO₂, (iv) 0.7CeO₂/Rh-SnO₂, (vi) 0.4CeO₂/Rh-In₂O₃). Source data are provided as a Source Data file.

N: ammonia, C: CO, and M: CH₄). **b** PCA plot generated using data obtained from a 3 × 3 sensor array exhibiting different partial selectivities to demonstrate aromatic BTEX gas discrimination over the interferences from ethanol, HCHO, acetone, ammonia, CO, and CH₄ (concentrations: 1–5 ppm). **c** PCA result constructed by data obtained from three major sensors ((iii) 0.4CeO₂/Rh-SnO₂, (iv) 0.7CeO₂/Rh-SnO₂, (vi) 0.4CeO₂/Rh-In₂O₃). Source data are provided as a Source Data file.

Fabrication of bilayer sensor with Rh-SnO₂ gas-sensing film and CeO₂ overlayer

The slurry for gas-sensing-film was prepared by mixing the Rh-SnO₂ spheres with a terpineol-based ink binder (Rh-SnO₂/binder = 30:70 w/w) and subsequently screen-printing the slurry onto an Al₂O₃ substrate with two Au electrodes (1.5 mm × 1.5 mm, electrode gap: 0.2 mm) (Supplementary Fig. 26b). The sensors were heated at 450 °C for 3 h to remove any residual organic components. Subsequently, catalytic CeO₂ overlayers were deposited onto the Rh-SnO₂ gas-sensing films by electron-beam evaporation under vacuum (base pressure: 5×10^{-6} Torr) (Supplementary Fig. 26c).

Data availability

The data that support Figs. 2–9 can be found in the Source Data, and the data that support the findings of this study are available from the corresponding author upon request. Source data are provided with this paper.

References

1. Jeong, S.-Y., Kim, J.-S. & Lee, J.-H. Rational design of semiconductor-based chemiresistors and their libraries for next-generation artificial olfaction. *Adv. Mater.* **32**, 2002075 (2020).
2. Röck, F., Barsan, N. & Weimar, U. Electronic nose: current status and future trends. *Chem. Rev.* **108**, 705–725 (2008).

3. Yang, Y.-C. Chemical detoxification of nerve agent VX. *Acc. Chem. Res.* **32**, 109–115 (1999).
4. Zhang, J., Liu, X., Neri, G. & Pinna, N. Nanostructured materials for room-temperature gas sensors. *Adv. Mater.* **28**, 795–831 (2016).
5. Yamazoe, N. Toward innovations of gas sensor technology. *Sens. Actuators, B* **108**, 2–14 (2005).
6. Sandhu, S. S. et al. Green MIP-202 (Zr) catalyst: degradation and thermally robust biomimetic sensing of nerve agents. *J. Am. Chem. Soc.* **143**, 18261–18271 (2021).
7. Lan, Q. et al. Hematotoxicity in workers exposed to low levels of benzene. *Science* **306**, 1774–1776 (2004).
8. Correa, S. M., Arbillal, G., Marques, M. R. & Oliveira, K. M. The impact of BTEX emissions from gas stations into the atmosphere. *Atmos. Pollut. Res.* **3**, 163–169 (2012).
9. Verma, D. K., Johnson, D. M. & McLean, J. D. Benzene and total hydrocarbon exposures in the upstream petroleum oil and gas industry. *Am. Ind. Hyg. Assoc. J.* **61**, 255–263 (2000).
10. Chen, Q. F., Milburn, R. K. & Karella, N. S. Real time monitoring of hazardous airborne chemicals: A styrene investigation. *J. Hazard. Mater.* **132**, 261–268 (2006).
11. Wang, B. et al. A highly sensitive diketopyrrolopyrrole-based ambipolar transistor for selective detection and discrimination of xylene isomers. *Adv. Mater.* **28**, 4012–4018 (2016).
12. Moon, Y. K., Kim, K. B., Jeong, S.-Y. & Lee, J.-H. Designing oxide chemiresistors for detecting volatile aromatic compounds: recent progresses and future perspectives. *Chem. Commun.* **58**, 5439–5454 (2022).
13. Loomis, D. et al. Carcinogenicity of benzene. *Lancet Oncol.* **18**, 1574–1575 (2017).
14. Durmusoglu, E., Taspinar, F. & Karademir, A. Health risk assessment of BTEX emissions in the landfill environment. *J. Hazard. Mater.* **176**, 870–877 (2010).
15. Sheu, R. et al. Human transport of thirdhand tobacco smoke: a prominent source of hazardous air pollutants into indoor non-smoking environments. *Sci. Adv.* **6**, eaay4109 (2020).
16. Wang, Z. et al. Highly sensitive and discriminative detection of BTEX in the vapor phase: a film-based fluorescent approach. *ACS Appl. Mater. Interfaces* **10**, 35647–35655 (2018).
17. Ionov, D. et al. Simple fluorescent sensor for simultaneous selective quantification of benzene, toluene and xylene in a multicomponent mixture. *Procedia Eng.* **168**, 341–345 (2016).
18. Kolmakov, A., Zhang, Y., Cheng, G. & Moskovits, M. Detection of CO and O₂ using tin oxide nanowire sensors. *Adv. Mater.* **15**, 997–1000 (2003).
19. Franke, M. E., Koplin, T. J. & Simon, U. Metal and metal oxide nanoparticles in chemiresistors: does the nanoscale matter? *Small* **2**, 36–50 (2006).
20. Ren, Y. et al. Synthesis of orthogonally assembled 3D cross-stacked metal oxide semiconducting nanowires. *Nat. Mater.* **19**, 203–211 (2020).
21. Kim, S.-J. et al. Mesoporous WO₃ nanofibers with protein templated nanoscale catalysts for detection of trace biomarkers in exhaled breath. *ACS Nano* **10**, 5891–5899 (2016).
22. Righetti, M., Amann, A. & Pratsinis, S. E. Breath analysis by nanostructured metal oxides as chemo-resistive gas sensors. *Mater. Today* **18**, 163–171 (2015).
23. Sysoev, V. V. et al. Single-nanobelt electronic nose: engineering and tests of the simplest analytical element. *ACS Nano* **4**, 4487–4494 (2010).
24. Park, S. Y. et al. Chemoresistive materials for electronic nose: progress, perspectives, and challenges. *Infomat* **1**, 289–316 (2019).
25. Jeong, S.-Y. et al. A general solution to mitigate water poisoning of oxide chemiresistors: bilayer sensors with Tb₄O₇ overlayer. *Adv. Funct. Mater.* **31**, 2007895 (2021).
26. Lee, J.-H. Linear gas sensing with dielectric excitation. *Nat. Electron.* **3**, 239–240 (2020).
27. Schroeder, V., Savagatrup, S., He, M., Lin, S. & Swager, T. M. Carbon nanotube chemical sensors. *Chem. Rev.* **119**, 599–663 (2019).
28. Yuan, W. & Shi, G. Graphene-based gas sensors. *J. Mater. Chem. A* **1**, 10078–10091 (2013).
29. Anichini, C. et al. Chemical sensing with 2D materials. *Chem. Soc. Rev.* **47**, 4860–4908 (2015).
30. Kim, S. J. et al. Metallic Ti₃C₂T_x MXene gas sensors with ultrahigh signal-to-noise ratio. *ACS Nano* **12**, 986–993 (2018).
31. Yoon, J.-W. et al. Trimodally porous SnO₂ nanospheres with three-dimensional interconnectivity and size tunability: a one-pot synthetic route and potential application as an extremely sensitive ethanol detector. *NPG Asia Mater.* **8**, e244–e244 (2016).
32. Jang, J.-S. et al. Heterogeneous, porous 2D oxide sheets via rapid galvanic replacement: toward superior HCHO sensing application. *Adv. Funct. Mater.* **29**, 1903012 (2019).
33. Zhou, X. et al. Porous ZnO/ZnCo₂O₄ hollow spheres: synthesis, characterization, and applications in gas sensing. *J. Mater. Chem. A* **2**, 17683–17690 (2014).
34. Jo, Y. K. et al. Exclusive and ultrasensitive detection of formaldehyde at room temperature using a flexible and monolithic chemiresistive sensor. *Nat. Commun.* **12**, 1–9 (2021).
35. Chen, R. et al. Unveiling the unconventional roles of methyl number on the ring-opening barrier in photocatalytic decomposition of benzene, toluene and o-xylene. *Appl. Catal. B* **278**, 119318 (2020).
36. Strini, A., Cassese, S. & Schiavi, L. Measurement of benzene, toluene, ethylbenzene and o-xylene gas phase photodegradation by titanium dioxide dispersed in cementitious materials using a mixed flow reactor. *Appl. Catal. B* **61**, 90–97 (2005).
37. Sui, L. et al. Au-loaded hierarchical MoO₃ hollow spheres with enhanced gas-sensing performance for the detection of BTX (benzene, toluene, and xylene) and the sensing mechanism. *ACS Appl. Mater. Interfaces* **9**, 1661–1670 (2017).
38. Liu, Y. et al. Hierarchical SnO₂ nanostructures made of intermingled ultrathin nanosheets for environmental remediation, smart gas sensor, and supercapacitor applications. *ACS Appl. Mater. Interfaces* **6**, 2174–2184 (2014).
39. Zhang, J. et al. Facile synthesis of mesoporous hierarchical Co₃O₄–TiO₂ p–n heterojunctions with greatly enhanced gas sensing performance. *J. Mater. Chem. A* **5**, 10387–10397 (2017).
40. Kang, H. et al. Multiarray nanopattern electronic nose (e-nose) by high-resolution top-down nanolithography. *Adv. Funct. Mater.* **30**, 2002486 (2020).
41. Zampolli, S. et al. Selectivity enhancement of metal oxide gas sensors using a micromachined gas chromatographic column. *Sens. Actuators B* **105**, 400–406 (2005).
42. Jeong, S.-Y. et al. Ultra-selective detection of sub-ppm-level benzene using Pd–SnO₂ yolk–shell micro-reactors with a catalytic Co₃O₄ overlayer for monitoring air quality. *J. Mater. Chem. A* **5**, 1446–1454 (2017).
43. Jeong, H.-M. et al. Gas selectivity control in Co₃O₄ sensor via concurrent tuning of gas reforming and gas filtering using nanoscale hetero-overlayer of catalytic oxides. *ACS Appl. Mater. Interfaces* **9**, 41397–41404 (2017).
44. Moon, Y. K. et al. Highly selective detection of benzene and discrimination of volatile aromatic compounds using oxide chemiresistors with tunable Rh-TiO₂ catalytic overlayers. *Adv. Sci.* **8**, 2004078 (2021).
45. Moon, Y. K., Jeong, S.-Y., Kang, Y. C. & Lee, J.-H. Metal oxide gas sensors with Au nanocluster catalytic overlayer: toward tuning gas

- selectivity and response using a novel bilayer sensor design. *ACS Appl. Mater. Interfaces* **11**, 32169–32177 (2019).
46. Hubálek, J. et al. Pt-loaded Al_2O_3 catalytic filters for screen-printed WO_3 sensors highly selective to benzene. *Sens. Actuators B* **101**, 277–283 (2004).
 47. Weber, I. C., Rüedi, P., Šot, P., Güntner, A. T. & Pratsinis, S. E. Handheld device for selective benzene sensing over toluene and xylene. *Adv. Sci.* **9**, 2103853 (2022).
 48. Bai, S., Xu, Y., Cao, K. & Huang, X. Selective ethanol oxidation reaction at the Rh– SnO_2 interface. *Adv. Mater.* **33**, 2005767 (2021).
 49. Huang, X. et al. Atomic-scale observation of the metal–promoter interaction in Rh-based syngas-upgrading. *Catalysts. Angew. Chem. Int. Ed.* **58**, 8709–8713 (2019).
 50. Liu, J. et al. Enhanced gas sensing properties of SnO_2 hollow spheres decorated with CeO_2 nanoparticles heterostructure composite materials. *ACS Appl. Mater. Interfaces* **8**, 6669–6677 (2016).
 51. Shin, J. et al. Thin-wall assembled SnO_2 fibers functionalized by catalytic Pt nanoparticles and their superior exhaled-breath-sensing properties for the diagnosis of diabetes. *Adv. Funct. Mater.* **23**, 2357–2367 (2013).
 52. Koffyberg, F. Optical bandgaps and electron affinities of semiconducting Rh_2O_3 (I) and Rh_2O_3 (III). *J. Phys. Chem. Solids* **53**, 1285–1288 (1992).
 53. Cho, Y. H., Liang, X., Kang, Y. C. & Lee, J.-H. Ultrasensitive detection of trimethylamine using Rh-doped SnO_2 hollow spheres prepared by ultrasonic spray pyrolysis. *Sens. Actuators B* **207**, 330–337 (2015).
 54. Bi, W., Wang, W. & Liu, S. Synthesis of Rh– SnO_2 nanosheets and ultra-high triethylamine sensing performance. *J. Alloy. Compd.* **817**, 152730 (2020).
 55. Na, C. W., Woo, H.-S., Kim, I.-D. & Lee, J.-H. Selective detection of NO_2 and $\text{C}_2\text{H}_5\text{OH}$ using a Co_3O_4 -decorated ZnO nanowire network sensor. *Chem. Commun.* **47**, 5148–5150 (2011).
 56. Xing, R. et al. Au-modified three-dimensional In_2O_3 inverse opals: synthesis and improved performance for acetone sensing toward diagnosis of diabetes. *Nanoscale* **7**, 13051–13060 (2015).
 57. Li, J. et al. Carbon nanotube sensors for gas and organic vapor detection. *Nano Lett.* **3**, 929–933 (2003).
 58. Kim, Y. H. et al. Chemically fluorinated graphene oxide for room temperature ammonia detection at ppb levels. *J. Mater. Chem. A* **5**, 19116–19125 (2017).
 59. Centers for Disease Control and Prevention (CDC). Immediately dangerous to life or health concentrations. <https://www.cdc.gov/niosh/idlh/71432.html> (1994).
 60. Centers for Disease Control and Prevention (CDC). Immediately dangerous to life or health concentrations. <https://www.cdc.gov/niosh/idlh/108883.html> (1994).
 61. Centers for Disease Control and Prevention (CDC). Immediately dangerous to life or health concentrations. <https://www.cdc.gov/niosh/idlh/100414.html> (1994).
 62. Centers for Disease Control and Prevention (CDC). Immediately dangerous to life or health concentrations. <https://www.cdc.gov/niosh/idlh/95476.html> (1994).
 63. Centers for Disease Control and Prevention (CDC). Immediately dangerous to life or health concentrations. <https://www.cdc.gov/niosh/idlh/100425.html> (1994).
 64. Han, H. J. et al. Synergistic integration of chemo-resistive and SERS sensing for label-free multiplex gas detection. *Adv. Mater.* **33**, 2105199 (2021).
 65. Delimaris, D. & Ioannides, T. VOC oxidation over MnOx-CeO_2 catalysts prepared by a combustion method. *Appl. Catal. B* **84**, 303–312 (2008).
 66. Kong, J., Xiang, Z., Li, G. & An, T. Introduce oxygen vacancies into CeO_2 catalyst for enhanced coke resistance during photothermocatalytic oxidation of typical VOCs. *Appl. Catal. B* **269**, 118755 (2020).
 67. Zhang, Y. et al. Investigation into the catalytic roles of oxygen vacancies during gaseous styrene degradation process via CeO_2 catalysts with four different morphologies. *Appl. Catal. B* **309**, 121249 (2022).
 68. Khan, M. E., Khan, M. M. & Cho, M. H. Ce^{3+} -ion, surface oxygen vacancy, and visible light-induced photocatalytic dye degradation and photocapacitive performance of CeO_2 -graphene nanostructures. *Sci. Rep.* **7**, 1–17 (2017).
 69. Yamazoe, N. & Shimane, K. Theoretical approach to the gas response of oxide semiconductor film devices under control of gas diffusion and reaction effects. *Sens. Actuators B* **154**, 277–282 (2011).
 70. Harrison, P. & Willett, M. The mechanism of operation of tin (IV) oxide carbon monoxide sensors. *Nature* **332**, 337–339 (1988).
 71. Kim, S. C. & Shim, W. G. Properties and performance of Pd based catalysts for catalytic oxidation of volatile organic compounds. *Appl. Catal. B* **92**, 429–436 (2009).
 72. Yang, C. et al. Abatement of various types of VOCs by adsorption/catalytic oxidation: a review. *Chem. Eng. J.* **370**, 1128–1153 (2019).
 73. Wang, Y. et al. Horseshoe-shaped SnO_2 with annulus-like mesoporous for ethanol gas sensing application. *Sens. Actuators B* **240**, 1321–1329 (2017).
 74. Ruminski, A. M., Moore, M. M. & Sailor, M. J. Humidity-compensating sensor for volatile organic compounds using stacked porous silicon photonic crystals. *Adv. Funct. Mater.* **18**, 3418–3426 (2008).
 75. Zhang, Y. et al. Self-assemblies of Pd nanoparticles on the surfaces of single crystal ZnO nanowires for chemical sensors with enhanced performances. *J. Mater. Chem.* **19**, 4701–4706 (2009).
 76. Wang, C. et al. Reduced graphene oxide decorated with CuO-ZnO hetero-junctions: towards high selective gas-sensing property to acetone. *J. Mater. Chem. A* **2**, 18635–18643 (2014).
 77. Kim, J.-H., Chun, J., Kim, J. W., Choi, W. J. & Baik, J. M. Self-powered, room-temperature electronic nose based on triboelectrification and heterogeneous catalytic reaction. *Adv. Funct. Mater.* **25**, 7049–7055 (2015).
 78. Jang, J.-S., Koo, W.-T., Choi, S.-J. & Kim, I.-D. Metal organic framework-templated chemiresistor: sensing type transition from P-to-N using hollow metal oxide polyhedron via galvanic replacement. *J. Am. Chem. Soc.* **139**, 11868–11876 (2017).

Acknowledgements

This work was supported by grants (Nos. 2021R1C1C2009461 and 2021M3H4A3A02086430) from the National Research Foundation (NRF) of Korea, funded by the Government of Korea (MSIT).

Author contributions

S.-Y.J. and Y.K.M. contributed equally to this work. S.-Y.J. supervised the project. S.-Y.J. and Y.K.M. conceived the concept and experiments. S.-Y.J. fabricated the gas-sensing materials and conducted structural characterization. Y.K.M. conducted gas-sensing tests and PTR-QMS analysis. J.W. and J.-H.L. were in charge and advised on all parts of the project. The manuscript is mainly written by S.-Y.J. All authors discussed the results and the manuscript at all stages.

Competing interests

The authors declare no competing interests.

Additional information

Supplementary information The online version contains supplementary material available at
<https://doi.org/10.1038/s41467-023-35916-3>.

Correspondence and requests for materials should be addressed to Seong-Yong Jeong.

Peer review information *Nature Communications* thanks the anonymous reviewer(s) for their contribution to the peer review of this work.

Reprints and permissions information is available at
<http://www.nature.com/reprints>

Publisher's note Springer Nature remains neutral with regard to jurisdictional claims in published maps and institutional affiliations.

Open Access This article is licensed under a Creative Commons Attribution 4.0 International License, which permits use, sharing, adaptation, distribution and reproduction in any medium or format, as long as you give appropriate credit to the original author(s) and the source, provide a link to the Creative Commons license, and indicate if changes were made. The images or other third party material in this article are included in the article's Creative Commons license, unless indicated otherwise in a credit line to the material. If material is not included in the article's Creative Commons license and your intended use is not permitted by statutory regulation or exceeds the permitted use, you will need to obtain permission directly from the copyright holder. To view a copy of this license, visit <http://creativecommons.org/licenses/by/4.0/>.

© The Author(s) 2023